Research Article
Journal of Geophysical Research: Oceans
DOI 10.1002/2014JC009869

# Spectral form and source term balance of short gravity wind waves

Hitoshi Tamura,[1] William M. Drennan,[2] Erik Sahlée,[3] and Hans C. Graber[2]

---

[1]Research Institute for Global Change,

Japan Agency for Marine-Earth Science and

Technology, Yokohama, Kanagawa, Japan

[2]Rosenstiel School of Marine and

Atmospheric Science, University of Miami,

Miami, Florida, USA.

[3]Department of Earth Sciences, Uppsala

University, Uppsala, Sweden

Received: Jan 29, 2014; Revised: Sep 21, 2014; Accepted: Oct 01, 2014

**Abstract.** We investigated the spectral structure and source term balance of short gravity waves, based on *in situ* observations of wavenumber spectra retrieved by air-sea interaction spar (ASIS) buoys. The behaviors of wavenumber spectra up to 10 rad/m (the gravity wave regime) were analyzed for a wide range of wind and wave conditions. The observed wavenumber spectra showed the spectral power laws described by *Toba* [1973] and *Phillips* [1958] in addition to the characteristic nodal point at ∼10 rad/m where spectral energy becomes constant over the entire wind speed range. We also improved the third-generation wave model using the nonlinear dissipation term. The wave model reproduced the spectral form in the higher wavenumber domain. In the equilibrium range, nonlinear transfer played a major role in maintaining equilibrium conditions. On the other hand, in the saturation range, which starts at the upper limit of the equilibrium range, the nonlinear transfer tended to be out of balance with other source terms, and the dissipation term was in balance with wind input.

## 1. Introduction

Ocean surface waves, from capillary waves to swells, vary greatly on a wide range of temporal and spatial scales. Whereas the contribution of small-scale surface waves to the total wave energy is negligible, they contribute significantly to aerodynamic roughness and air-sea interaction processes, such as momentum transfer and gas exchange between the atmosphere and ocean. The modeling and analysis of microwave backscatter captured by scatterometers is significantly dependent on knowledge of the spectral characteristics of short gravity waves and gravity-capillary waves. Therefore, a better understanding of the spectral structure of small-scale ocean surface waves is crucial.

The spectral shape and wind speed dependence of spectral energy vary with wavenumber. The spectral structure in the equilibrium range has been addressed in a number of studies for wavenumbers ranging up to ∼1 rad/m (6.3 m in wave length), or roughly three times the typical peak frequency. Nowadays, a spectral form of $F(k) = \alpha_4 u_* g^{-1/2} k^{-5/2}$ (where, $F(k)$ is the omnidirectional surface elevation spectrum in the wavenumber domain, $k$ is the wavenumber, $g$ is the gravitational acceleration, and $u_*$ is the friction velocity) in this range is commonly seen as robust in the ocean [e.g., *Toba*, 1973; *Donelan et al.*, 1985; *Resio et al.*, 2004]. *Banner et al.* [1989] analyzed the wavenumber spectra ranging from 4 to 31 rad/m, which are much shorter than the spectral components in the equilibrium range. They concluded that $u_*$ dependence of the spectral energy might be neglected, and the wavenumber spectrum can be represented by $F(k) = \alpha_5 k^{-3}$ to the lowest-order approximation. This form was originally proposed by the pioneering work of *Phillips* [1958], and *Forristall* [1981] also described a transition of the spectral power law from $k^{-5/2}$ to $k^{-3}$. The backscattered power of L-band microwaves (wavenumber: 27 rad/m, wavelength: 0.24 m) shows weak dependence on surface wind [e.g., *Isoguchi and Shimada*, 2009]. Evidence consistently suggests that the spectral density in the intermediate range (∼5-30 rad/m) barely responds to the surface wind, because the backscattered power is basically proportional to the spectral density of the Bragg waves.

In the present study, we investigated the characteristics of the spectral structure for short gravity waves. In particular, we were interested in furthering the understanding of the dynamic balance of three source terms: wind input, nonlinear spectral transfer, and dissipation. We used observations from two campaigns in which wind velocities and surface elevations were measured by air-sea interaction spar (ASIS) buoys [*Graber et al.*, 2000]. We investigated the behavior of observed wavenumber spectra up to 10 rad/m (the gravity wave regime) for a wide range of wind and wave conditions. We also conducted wave hindcasts to validate the applicability of the 3rd generation wave model and to discuss spectral forms and source term balances in the short gravity wave regime. It should be noted that the wavenumber range larger than the gravity-capillary wave regime ($\sim 10^2 - 10^3$ rad/m) is beyond the scope of the present study.

The remainder of the paper is organized as follows. Section 2 describes the *in situ* datasets of wind and surface waves analyzed in this study. The model configurations of wave hindcasts are described in Section 3. In Section 4, we show the observational and model results in terms of wavenumber spectra in short gravity wave regimes. Then we discuss the spectral form and source term balance using hindcast experiments in Section 5. Finally, a summary is provided in Section 6.

## 2. *In situ* data and analysis method

Traditionally many studies of surface gravity waves have relied on frequency spectra estimated from time series of surface elevation. However, as reported by *Hwang and Wang* [2004] and elsewhere, the Doppler frequency shift of short waves being convected by surface current (and longer waves) can cause serious problems in the interpretation of short wave spectra. For this reason, the study of short waves is best carried out with wavenumber spectra, calculated from spatial data. These data include those collected from stereophotography [*Banner et al*, 1989], sparse spatial arrays [*Donelan et al*, 1985] or radar backscatter [e.g. *Hwang and Plant*, 2010]. Such data are difficult to obtain, hence are relatively rare. Here, we apply the wavelet directional method (WDM) proposed by *Donelan et al.* [1996] to get wavenumber spectra directly from the time series of surface elevations from wave staff arrays. The WDM provides the instantaneous local wavenumber vector and the corresponding wave energy with the assumption that at most one wave of a given scale propagates through the array at a given time. Following *Donelan et al.* [1996], we used the Morlet wavelet, with eight voices. Mean wavenumber spectra were estimated by binning the averages of the wavelet spectrum at each instance in time. *Donelan et al* [1996] showed that frequency-directional spectra calculated by the wavelet method compared well to those calculated by traditional Fourier analysis and the Maximum Likelihood Method. Here we focus on 1D (non-directional) wave number spectra calculated by WDM.

We used wind and wave data from the FETCH (flux, etat de la mer et télédétection en Conditions de fetch variable) experiment [*Hauser et al.*, 2003] and the DOGEE (Deep

Ocean Gas Exchange Experiment) [*Brooks et al.*, 2009]. The details of the wind and wave data retrieved in the two field campaigns are described below.

### 2.1. The FETCH data sets

The FETCH experiment took place from March to April (Year Day YD: 77-99) 1998, in the Gulf of Lion, Mediterranean Sea. During the FETCH campaign, an ASIS buoy [*Graber et al.*, 2000] was deployed at 42.98°N, 04.25°E (roughly 50 km SSW of the Rhone delta, at a depth of 100 m) to measure the temporal evolution of turbulent momentum fluxes (or friction velocity) and the surface gravity waves. The study site is well known for frequent strong northerly events [e.g., *Sampe and Xie*, 2007], known as Mistrals. During the observation period, the surface wind field was dominated by Mistral events from YD 78.8-81.2, and from YD 83-84.5 [*Drennan et al.*, 2003]. The temporal changes in surface elevations were obtained from an array of six capacitance wave staffs arranged in a centered pentagon of radius 0.927 m. The sampling rate was 12 Hz and wind and wave parameters were calculated from data segments of 28.5 min. A full description of the data collection and processing is provided by *Drennan et al.* [2003]. We analyzed a total of 857 wind and wave datasets. The highest wavenumber analyzed was 1 rad/m (wave length: 6.3m).

### 2.2. DOGEE data sets

Wind and wave data were also collected during DOGEE (Cruise D320) from June 22 to July 11 (YD: 173-192) 2007 in the northeast Atlantic. An ASIS buoy was configured for Lagrangian measurements (i.e., free drifting) and deployed at 43.753°N, 18.116°W, at a depth of ∼4000 m. The wavenumber spectra were obtained from an array of four capacitance wave staffs placed in a square with sides of 0.2 m. The array was on an outrigger 2.6 m away from the ASIS buoy to eliminate possible contamination due to the main 0.2 m diameter spars of the buoy. Data were sampled continuously at 20 Hz and wind and wave parameters were calculated from data segments of 30 min. The phase differences detected by wave staffs were used to provide the wavenumber vector in the WDM. Due to the shorter spacing behavior (0.2 m) of the capacitance wave staffs, it was difficult to detect the propagation (i.e., phase difference) of longer waves. Therefore, the lowest and highest wave numbers analyzed were set at 1 (wave length: 6.3 m) and 10 rad/m (wave length: 0.63 m), respectively. The observed wavenumber spectra were significantly contaminated by the overtopping of wave staffs during a severe storm from YD 180.7-182.6. After YD 183.2, two of the wave gauges were broken. We do not use any data following the storm event. A total of 352 wavenumber spectra were available for analysis.

## 3. Wave hindcasts

The spectral evolution of surface gravity waves can be represented by the following wave action equation:

$$D_t N = S_{in} + S_{nl} + S_{ds} \tag{1}$$

where $D_t = \partial_t + c_g \cdot \nabla_x$ is the material derivative, $c_g$ is the group velocity, $\theta$ is wave direction, $N = N(k, \theta)$ is the wave action ($= F(k, \theta)/\sigma$, where $\sigma$ is the intrinsic frequency) with units of m$^3$s, $S_{in}$ is wind input, $S_{ds}$ is wave dissipation, and $S_{nl}$ is the nonlinear transfer function. To discuss the spectral shape in the higher wavenumber domain, we also used the saturation spectrum, $B(k)$, defined as:

$$B(k) = k^3 F(k) = k^3 \int_{-\pi}^{\pi} \Psi(k, \theta) k d\theta \tag{2}$$

where $\Psi(k,\theta)$ is the wavenumber spectrum in polar form with units of m$^4$. Wave hindcasts were conducted based on WAVEWATCH-III$^{\mathrm{TM}}$ ver.3.14 [WW3; *Tolman*, 2009]. The spectral space was discretized using 40 frequencies, ranging from 0.0412 to 3.995 Hz (relative frequency of 10 %, $f_{m+1} = 1.1 f_m$), with 36 directions ($\Delta\theta = 10°$). The corresponding wavenumber range was $6.8\times10^{-3}$–$6.24\times10^{1}$ rad/m. Because one of our objectives was to investigate the spectral shape in the higher wavenumber region, we did not apply the diagnostic parameterization of the spectral tail. In addition, the minimum time step for source terms integration is set to be very small (1 second) to allow very small variation of wave spectra in higher wavenumber domain. *Tolman and Chalikov*'s [1996] (hereafter, TC96) source terms were used for $S_{in}$ and $S_{ds}$. TC96 defined the dissipation terms of the lower and higher wavenumber domains separately. The wave energy dissipation in the higher wavenumber domain, $S_{ds}^{high}$, can be derived semi-empirically from the source term balance between $S_{ds}^{high}$ and $S_{in}$, and is expressed with the saturation spectrum, $B(k)$:

$$S_{ds}^{high} = -a_0'(u_*/c)^2 k^{-3} B^{\beta+1}(k,\theta) \tag{3}$$

$$\beta = a_1'(u_*/c)^{-a_2} \tag{4}$$

where $a_0'$, $a_1'$ and, $a_2$ are non-dimensional tuning parameters, $c$ is the wave phase speed, and $\beta$ represents the nonlinearity of the dissipation term. Recent studies have indicated that the effect of nonlinearity on the dissipation term is important for accurate representation of observed wavenumber spectra in the high wavenumber domain [e.g., *Donelan et al.*, 2012, *Babanin et al.*, 2010]. This point is addressed in more detail in Section 5 with modification of the $S_{ds}^{high}$ term (Equation 3). We employed the discrete interaction approximation (DIA) method as the $S_{nl}$ [*Hasselmann et al.*, 1985]. Other source terms, such as linear input and bottom friction, were not used for the hindcast. The other computational parameters for the two experiments (FETCH and DOGEE) are summarized in Table 1. The wave model was driven by 6-hourly surface winds from the National Centers for Environmental Prediction/Climate Forecast System Reanalysis (NCEP/CFSR) product [*Saha et al.*, 2010], in which the global surface data set has a resolution of ∼38 km (Gaussian Grid: T382). Two-minute gridded elevations/bathymetry for world data (ETOPO2v2 Global Gridded Two-minute Database, National Oceanic and Atmospheric Administration, http://www.ngdc.noaa.gov/mgg/global/etopo2.html) was used to define the bottom topography and coastal lines. Hourly hindcast results were stored and statistical parameters and wave spectra at the observational location during the FETCH and DOGEE experiments were analyzed.

## 4. Results

### 4.1. Wind and wave conditions

The two datasets analyzed in this study show the characteristic features of surface wave fields, depending on the surface wind and geometrical fetch. Figure 1 shows probability density functions (pdf) for various parameters. During the Mistral events, maximum wind speeds ($U_{10}$) reached ∼18 m/s, and the pdf of the surface wind speed was widely distributed for the FETCH experiment (Figure 1a). Despite the strong wind, the maximum significant wave height ($H_s$) during FETCH was limited to ∼3 m (Figure 1b), and the peak wave period $T_p$ was distributed around 6 s due to the fetch-limited wave growth (Figure 1c). On the other hand, because of the prominent westerlies and the limited data available for DOGEE, the pdfs of $U_{10}$ and $H_s$ were narrower, but maximum $U_{10}$ and $H_s$ were around 14 m/s and 3 m, respectively. Accordingly, the wave dataset for FETCH represents young windsea in the ocean, whereas the dominant sea state was a mature sea for DOGEE, which can also be confirmed in the pdf of inverse wave age (Figure 1d). The two datasets cover a wide range of sea states and represent the wavenumber spectra in open ocean conditions.

### 4.2. The spectral form and wind dependence

Figure 2 shows the saturation spectra, $B(k)$, plotted against wind speed for six different wavenumbers. Observed $B(k)$ values for FETCH (blue dots) were plotted for wavenumbers ranging from 0.2 to 1 rad/m. For DOGEE (red dots), the wavenumbers range from 1 to 10 rad/m, due to the difference in wave gauge arrangements (spatial resolution). $B(k)$ measured in different sea states were quantitatively consistent at $k = 1$ rad/m. Our evidence suggests that the estimated wavenumber spectra were robust, especially for short gravity wave regimes, and the WDM used for retrieving $F(k)$ functioned reasonably well for the estimation. Both datasets showed that $B(k)$ at $k = 1$ rad/m linearly increased with $U_{10}$ when wind speed was less than 10 m/s. For both datasets, $B(k)$ at $k$=1 rad/m tended to be saturated under higher winds. On the other hand, $B(k)$ in the intermediate range ($5 < k < 10$) showed a weak dependence on $U_{10}$ over the entire wind speed range.

We compared the $B(k)$ proposed by *Hwang* [2008] (the so-called H1 and H4 spectra in *Hwang and Plant*, 2010) and *Elfouhaily et al.* [1997] (hereafter, E spectrum) with the observations in Figure 2. Between the various models, there was a large discrepancy in representing the wavenumber spectrum, especially in the intermediate range of $1 < k < 10$ rad/m (refer to Figure 1 in *Hwang and Plant*, 2010). For example, *Hwang* [2008] proposed different spectral forms for conditions with (H4 spectrum) and without (H1 spectrum) background swells. The spectral energy of the H1 spectrum weakly increases with increasing surface wind for windsea conditions, whereas it is suppressed against increasing wind for swell dominant conditions (H4 spectrum). The H1 and H4 spectra both capture the linear increase in $B(k)$ for the lower wavenumber domain ($k < 1$ rad/m), but only the H4 spectrum portrays the weak dependence of $B(k)$ on wind speed at $k = 10$ rad/m. The E spectrum shows similar behavior for the whole wavenumber range (0.2-10 rad/m); strong saturation patterns and local maxima of the spectral density for middle wind speeds ($U_{10}$: 5-10 m/s), which was not confirmed by observation.

In Figure 3, the mean saturation spectra for each wind speed range are shown during the FETCH experiment. The observed wave spectra (Figure 3a) clearly show the characteristic spectral shape and its wavenumber power transition. When the wind speed is greater than 14 m/s, we see the following: an overshoot near the spectral peak ($k$: 0.1-0.2 rad/m) [e.g., *Barnett and Willkerson*, 1967; *Hasselmann et al.*, 1973] and a subsequent $k^{-5/2}$ tail [e.g., *Donelan et al.*, 1985]. The spectral shape transition from $k^{-5/2}$ ($B(k) \sim k^{1/2}$) to $k^{-3}$ ($B(k) \sim k^{0}$) [*Forristall*, 1981] is also shown in Figure 3a. When the wind speed is less than 10 m/s, the overshoot and $k^{-3}$ tail are not easily discernible. Interestingly, the spectral bandwidth in which the $k^{-2.5}$ power law appears depends on the wind speed; the bandwidth is broader for lower wind speeds ($U_{10} < 10$ m/s) and narrower for higher wind speeds ($U_{10} > 10$ m/s).

Third-generation wave models provide the most powerful tools for investigating the energy-containing region (the spectral peak) in the wavenumber domain, because they describe the temporal and spatial evolution of the wave spectrum without any prior assumptions about spectral shape. WW3 can reproduce the peak value of the overshoot and the spectral shape near the peak region ($k$: 0.1-0.3 rad/m), as shown in Figure 3b. On the other hand, modeled $B(k)$ deviates substantially from observations in the higher wavenumber domain ($k$: 0.5-1 rad/m), where a diagnostic spectral tail is usually attached ($B(k) \sim k^0$, in the default settings of WW3). There was no clear overshoot and no wind speed dependence of the spectral shape in either the E spectrum with a 50 km fetch (Figure 3c) or the H1 spectrum (Figure 3d). This is because the spectral evolution near the peak region is strongly dependent on the temporal and spatial variation in the surface wind fields, such as the Mistrals, which cannot be taken into account in the E and H1 spectra.

Figure 4 shows the mean saturation spectra for the DOGEE. Observed spectra (Figure 4a) were quantitatively very consistent with *Banner et al.* [1989]; that is, the wind speed dependence of $B(k)$ was weak (see also Figure 2) and the power law of $B(k)$ was mainly confined to between $k^0$ and $k^{0.18}$ in the wavenumber range of 2-10 rad/m. Moreover, the value of $B(k)$ eventually became independent of the wind speed and showed the characteristic nodal point of saturation spectra at 10 rad/m, which can be seen in the H4 spectrum (Figure 4d). The E spectrum (Figure 4c) showed near-constant values of $B(k)$ and its weak dependence on wind speed in the wavenumber range of 1-10 rad/m. However, the spectral shape is different from those of *Banner et al.* [1989] and our observations (Figure 4a). In addition, WW3 (Figure 4b) could not reproduce the observed spectra in this wavenumber domain, where $B(k)$ is significantly overestimated and is proportional to the $k^{-5/2}$ shape.

### 4.3. Swell influence on short gravity waves

The spectral evolution of short waves riding on long waves is complicated because, in addition to wind influences, the short waves are modulated by the longer waves (e.g., Longuet-Higgins and Stewart, 1960) and wave breaking is enhanced, as the short waves may break on the crest of the long waves. Following *Smedman et al.* [2003], *Hwang* [2008], and *Sahlée et al.* [2012], we separated swell energy from windsea components and investigated the influence of swells on short gravity waves. *Hwang* [2008] defined the swell index $Svar$ as the ratio of the spectral energy in the frequency bands lower than the reference frequency, $\sigma_r$, to the spectral energy in the frequency bands higher than $\sigma_r$, where $\sigma_r$ is the higher value between the measured spectral peak frequency, $\sigma_p$, and the empirical peak frequency, $\sigma_0 = g/(1.2U_{10})$. Figure 5 shows the temporal variation in wind and wave parameters retrieved from the DOGEE dataset. The temporal variation in $B(k)$ at $k = 10$ rad/m was smaller than that at $k = 1$ rad/m (Figure 5c) and its correspondence to the wind speed was very weak, as shown in Figure 2. Swell energy was significant during YD 177-179, and YD 182.6-183.2 (Figure 5a) and the corresponding spectral bandwidth was narrow (Figure 5b). Figure 6 shows the variation in the 2.5 h running average $B(k{=}10$ rad/m) plotted against $Svar$. Clearly, $B(k)$ values decreased in significant swell conditions. The $B(k = 10$ rad/m) values showed a similar pattern when plotted against an alternate parameter, defined as the swell energy at wavenumbers less than 0.1 rad/m (not shown). *Hwang* [2008] proposed different spectral forms for when swells were present or absent; only when the swell effect was significant did the characteristic nodal point of the saturation spectra appear at wavenumber 10 (rad/m). On the other hand, our observations suggest that the spectral energy at $\sim k = 10$ rad/m was almost constant, but short wave energy decreased when significant swells existed.

## 5. Discussion

### 5.1. Spectral evolution and nonlinear dissipation terms

Wavenumber spectra $F(k)$ observed by ASIS buoys clearly showed different spectral forms in different wavenumber domains and the transition from $k^{-2.5}$ to $k^{-3}$, which is consistent with *Forristall* [1981], *Hwang and Wang* [2001], *Resio et al.* [2004] and *Long and Resio* [2007]. This suggests that different physical properties exist in the different wavenumber domains. The estimated spectra by WW3 showed a $k^{-2.5}$ form in the higher wavenumber domain (Figure 4b), which was different from our observations (Figure 4a). What causes this difference in spectral shape?

In the default settings of WW3, the diagnostic spectral tail of the $k^{-3}$ form is attached beyond nine times the peak wavenumber. Therefore, the $S_{ds}^{high}$ term (Equation 3) does not affect any spectral form in the higher wavenumber domain. In addition, because WW3 focuses on modeling the spectral peak region, parameterization of $\beta$ (Equation 4) in the wavenumber range of 1-10 rad/m is not taken into consideration. However, this range is the primary concern of this study, and if we calculate $\beta$, its parameters are $10^{-2}$-$10^{-1}$ for stronger winds (∼20 m/s) and $10^{-1}$-$10^{0}$ for weaker winds (∼5 m/s), suggesting a very weak dependence of nonlinearity, especially for moderate to high wind speeds.

Recent studies have proposed new source terms that include dissipation parameterizations [e.g., *Ardhuin et al.*, 2010; *Rascle and Ardhuin* , 2012; *Thomson et al*, 2013]. It is interesting to speculate that nonlinear dissipation is crucial for accurate representation of the spectral form in the higher wavenumber domain. *Donelan* [2001] (hereafter, D01) proposed the nonlinear dissipation function to balance wind input and dissipation due to wave breaking as follows:

$$S_{ds} = -A_2[(1 + A_3\ mss(k))^2 B(k)]^{2.5} k^{-3} B(k) \tag{5}$$

$$mss(k) = \int_0^k F(k)k^2 dk \tag{6}$$

where $A_2$ and $A_3$ are empirical coefficients [*Donelan et al*, 2012], and $mss$ is the integrated mean square slope, which was introduced to represent the modulation of short waves and enhanced breaking (spilling) due to the orbital motion of long waves. This dissipation form is currently being applied to wave models to estimate higher wavenumber spectra and related wind stress [ *Babanin et al.*, 2010; *Donelan et al.*, 2012]. In contrast to TC96, strong nonlinearity is included in the dissipation term, which effectively damps spectral growth in the higher wavenumber domain.

### 5.2. Wave hindcasts with nonlinear dissipation terms

We conducted three additional wave hindcasts for the DOGEE with nonlinear dissipation terms to validate the applicability of the nonlinear dissipation term. Wind input, $S_{in}$, and the wave energy dissipation in the lower wavenumber domain, $S_{ds}^{low}$, were the same as in TC96. In the first experiment, $S_{ds}^{high}$, as described by TC96 (Equation 3), was modified to reflect the strong nonlinear behavior; the nonlinear dependence of dissipation term on $B(k)$ (i.e., $\beta$+1 in Equation 3) was set at 3 (Exp1: $S_{in}^{TC96} + S_{ds}^{mTC96} + S_{nl}^{DIA}$). In the second experiment, the nonlinear dissipation term proposed by D01 was applied (Exp2: $S_{in}^{TC96} + S_{ds}^{D01} + S_{nl}^{DIA}$). Tunable parameters for both hindcasts were as follows: (Exp1) $a_0' = 0.35$, $\beta = 2.0$ in Equation 3; (Exp2) $A_2 = 5.8$, $A_3 = 132.0$ in Equation 5. In the third experiment, we employed an exact $S_{nl}$ term estimated using the WRT method [e.g., *Van Vledder*, 2006] (Exp3: $S_{in}^{TC96} + S_{ds}^{D01} + S_{nl}^{WRT}$). Due to the high computational cost for this experiment, we set a subdomain (40.8°N-44.8°N, 19°W-15°W) which is embedded in the model domain for DOGEE (0°-70°N, 100°W-15°E). The horizontal and spectral resolutions were same as for other experiments and the output spectra of Exp2 was used for the boundary condition of Exp3.

Figure 7 shows the saturation spectra for the three hindcast scenarios. All three models improved the spectral shape in the higher wavenumber domain; the spectral form tended to be saturated against the surface wind and exhibited $B(k) \sim k^0$ instead of $B(k) \sim k^{0.5}$ (Figure 4b). The spectral nodal point at $k = 10$ rad/m was also represented in all three models. However, in Figure 7a (Exp1), the overshoot of $B(k)$ was confirmed in the wavenumber range of 1-10 rad/m, whereas Exp2 (Figure 7b) and Exp3 (Figure 7c) performed significantly better and demonstrated the weak dependence of $B(k)$ on wind speed. We also conducted hindcast experiments of Exp1 with larger values of $\beta$ (2-4) in Equation 3, but the spectral form showed a similar trend, suggesting that the role of $mss$ is important for accurate representation of the observed spectra. Recently, the modulation of short waves by the underlying long waves has been widely studied, and from the modeling point of view, it is now seen as a cumulative dissipation [e.g., *Babanin et al.*, 2010]. Our results also support the importance of the cumulative effect, in terms of enhanced breaking, for accurate representation of observed wave spectra in the higher wavenumber range.

The difference between Exp2 and Exp3 comes from the estimation of the $S_{nl}$ term (i.e., DIA method vs. WRT method). The resonant four-wave interactions estimated by DIA are not well established [e.g., *Van Vledder et al.*, 2000; Tamura et al, 2008], and have not been validated in the higher wavenumber domain. Therefore, the applicability of DIA is unclear. However, the results (Figure 7b and 7c) showed similar behavior, implying that DIA was able to adequately reproduce the observation, but in the following discussions, we utilize the hindcast results from Exp3, which adequately represented the saturation spectrum in the higher wavenumber domain. Furthermore, we used an accurate method for evaluating $S_{nl}$, which should lead to reliable discussions of the source term balance.

### 5.3. Spectral form and source term balance

To maintain a stable spectral form in the higher wavenumber domain, the sum of the three source terms, $S_{total}$ (i.e., the right side of Equation 1), approaches zero during wave growth. This is called the equilibrium condition. We compared the net external force, $S_f(= S_{in} + S_{ds})$, and the nonlinear transfer function, $S_{nl}$, for different wavenumber ranges to confirm the source term balance. Figures 8 and 9 show the scatterplots of $S_{nl}$ and $S_{total}$, respectively, as a function of $S_f$, which were averaged for the wavenumber bins (a) 1-2 rad/m, (b) 10-20 rad/m, and (c) 30-40 rad/m. The results clearly demonstrate the different source term balance between $S_f$ and $S_{nl}$ for different wavenumber ranges; that is, $S_{nl}$ was in balance with $S_{nl}$ to cancel out the total source term for the wavenumber range of $\sim$ 1-2 rad/m (Figures 8a and 9a), whereas they were unbalanced in the higher wavenumber domain of 30-40 rad/m (Figure 8c). We observe that $S_f$ tends to approach $S_{total}$ (Figure 9c).

*Hwang and Wang* [2001] revisited the concept of a saturation range in which the $F(k) \sim k^{-3}$ form appeared. They treated the saturation range separately from the equilibrium range, and the saturation range started at the upper limit of the equilibrium range, according to the discussion of the *mss*. Here, we also separated the equilibrium range and saturation range, according to the role of $S_{nl}$ in source term balance (Figure 10). In the equilibrium range (Figure 8a), $S_{nl}$ played a major role in the adjustment of the total source term balance during wave evolution, and the equilibrium condition was maintained by the $S_{nl}$ [*Tamura et al.*, 2010]. In addition, as described by *Resio et al.* [2004], any net gain or loss of wave energy within the equilibrium range tends to force the spectrum away from a $k^{-2.5}$ shape. If the net force of $S_f$ is negligible within the equilibrium range, the spectrum should have a $k^{-2.5}$ form. This is again consistent with our hindcast results. The spectral form of $k^{-3}$ appeared in the equilibrium range (Figure 7c: $U_{10} > 8m/s$) where the net external force $S_f$ was negative (Figure 8a). When $U_{10}$ was less than 6 m/s, the spectral form approached the $k^{-2.5}$ shape and the $S_f$ values approached zero (Figure 8a). However, $S_{nl}$ tended to be out of balance with $S_f$ in the saturation range (Figure 8c). $S_f$ approached the total source term when the $S_{nl}$ term was not significant compared to $S_f$ (Figure 9c), implying that the $S_{ds}$ term was in balance with the $S_{in}$ term in this wavenumber range.

## 6. Summary

We investigated the characteristics of the spectral form for short gravity waves. In addition, to understand the dynamic balance of three sources, we conducted wave hindcasts with different dissipation terms. The observed wave spectra clearly showed the characteristic spectral shape and its wavenumber power transition; that is, the overshoot near the spectral peak and the subsequent spectral form transition from $k^{-2.5}$ to $k^{-3}$ in the higher wavenumber domain, which is consistent with previous research. At the wavenumber $k = 10$ rad/m, the saturation spectrum $B(k)$ became constant over the entire wind speed range. The WAVEWATCH-III model reproduced the spectral form in the peak region, whereas it deviated substantially from observations in the higher wavenumber domain. The nonlinear dissipation term, with enhanced breaking due to longer waves (the cumulative effect), significantly improved the model results. In the equilibrium range, the nonlinear transfer function, $S_{nl}$, played a major role in maintaining the equilibrium conditions. The spectral form $F(k)$ approached $k^{-3}$ for negative values of $S_f$, whereas it approached $k^{-2.5}$ for negligible $S_f$. On the other hand, in the saturation range, the spectral form approached $k^{-3}$, and $S_{nl}$ did not balance with the other source terms. The $S_{ds}$ term was in balance with $S_{in}$ in this wavenumber range.

**Acknowledgments.** We are grateful to three anonymous reviewers for their careful reading of this paper and their constructive comments, which were very helpful in improving the manuscript. The source code of WAVEWATCH-III$^{\text{TM}}$ ver.3.14 was provided by the Environmental Modeling Center at the National Centers for Environmental Prediction (http://polar.ncep.noaa.gov/waves/wavewatch/wavewatch.shtml). The surface winds for hindcast experiments were obtained from the National Centers for Environmental Prediction/Climate Forecast System Reanalysis (http://rda.ucar.edu/pub/cfsr.html). This work is part of the Japan Coastal Ocean Predictability Experiment (JCOPE) supported by the Japan Agency for Marine-Earth Science and Technology (JAMSTEC). HT in this work was supported by JSPS KAKENHI Grant Number 24760403. WD acknowledges the National Science Foundation (OCE-0623450) for support during DOGEE.

## References

Ardhuin, F., E. Rogers, A.V. Babanin, J. Filipot, R. Magne, A. Roland, A. Westhuysen, P. Queffeulou, J. Lefevre, L. Aouf, F. Collard (2010), Semiempirical Dissipation Source Functions for Ocean Waves. Part I: Definition, Calibration, and Validation, *J. Phys.*

*Oceanogr.*, *40*, 1917–1941, doi:doi:http://dx.doi.org/10.1175/2010JPO4324.1.

Babanin, A. V., K. N. Tsagareli, I. R. Young, D. J. Walker (2010), Numerical Investigation of Spectral Evolution of Wind Waves. Part II: Dissipation Term and Evolution Tests, *J. Phys. Oceanogr.*, *40*, 667–683, doi:http://dx.doi.org/10.1175/2009JPO4370.1.

Banner, M. L., I. S. F. Jones, and J. C. Trinder (1989), Wavenumber spectra of short-gravity waves, *J. Fluid Mech.*, *198*, 321–344, doi: http://dx.doi.org/10.1017/S0022112089000157.

Barnett, T. P., and J. C. Wilkerson (1967), On the generation of ocean wind waves as inferred from airborne radar measurements of fetch-limited spectra, *J. Mar. Res.*, *25*, 292–321.

Brooks, Ian M., and Coauthors (2009), Physical Exchanges at the Air-Sea Interface: UK-SOLAS Field Measurements. *Bull. Amer. Meteor. Soc.*, *90*, 629–644, doi: http://dx.doi.org/10.1175/2008BAMS2578.1

Donelan, M. A. (2001), A nonlinear dissipation function due to wave breaking, paper presented at Workshop on Ocean Wave Forecasting, Eur. Cent. for Med.-Range Weather Forecasts, Reading, U. K., 2-4 July.

Donelan, M. A., J. Hamilton, and W. H. Hui (1985), Directional spectra of wind-generated waves, *Philos. Trans. R. Soc. London, Ser. A*, *315*, 509–562, doi:10.1098/rsta.1985.0054.

Donelan, M. A., M. Curcic, S. S. Chen, and A. K. Magnusson (2012), Modeling waves and wind stress, *J. Geophys. Res.*, *117*, C00J23, doi:10.1029/2011JC007787.

Donelan, M. A., W. M. Drennan, and A. K. Magnussen (1996), Nonstationary analysis of the directional properties of propagating waves, *J. Phys. Oceanogr.*, *26*, 1901–1914.

Drennan, W. M., H. C. Graber, D. Hauser, and C. Quentin (2003), On the wave age dependence of wind stress over pure wind seas, *J. Geophys. Res.*, *108*(C3), 8062, doi: 10.1029/2000JC000715.

Elfouhaily, T., B. Chapron, K. Katsaros, and D. Vandemark (1997), A unified directional spectrum for long and short wind]driven waves, *J. Geophys. Res.*, *102*, C7, 15,781–15,796, doi:10.1029/97JC00467.

Forristall, G. Z. (1981), Measurements of a saturated range in ocean wave spectra, *J. Geophys. Res.*, *86*, C9, 8075–8084, doi:10.1029/JC086iC09p08075.

Graber, H. C., E. A. Terray, M. A. Donelan, W. M. Drennan, J. Van Leer, and D. B. Peters (2000), ASIS -A new air-sea interaction spar buoy: Design and performance at sea, *J. Atmos. Oceanic Technol.*, *17*, 708–720.

Hasselmann, K., T. P. Barnett, E. Bouws, H. Carlson, D. E. Cartwright, K. Enke, J.A. Ewing, H. Gienapp, D. E. Hasselmann, P. Kruseman, A. Meerburg, P. Muller, D.J. Olbers, K. Richter, W. Sell, and H. Walden (1973), Measurements of wind wave growth and swell decay during the Joint North Sea Wave Project (JONSWAP), *Dt. Hydrogr. Z.*, A8 (12), 95 pp.

Hasselmann, S., K. Hasselmann, J. H. Allender, and T. P. Barnett (1985), Computations and parameterizations of the nonlinear energy transfer in a gravity-wave spectrum. Part II: Parameterizations of the nonlinear energy transfer for application in wave models, *J. Phys. Oceanogr.*, *15*, 1378–1391.

Hauser, D., et al. (2003), The FETCH experiment: An overview, *J. Geophys. Res.*, *108*(C3), 8053, doi:10.1029/2001JC001202.

Hwang, P. A. (2008), Observations of swell influence on ocean surface roughness, *J. Geophys. Res.*, *113*, C12024, doi:10.1029/2008JC005075.

Hwang, P. A., and D. W. Wang (2001), Directional distributions and mean square slopes in the equilibrium and saturation ranges of the wave spectrum, *J. Phys. Oceanogr.*, *31*, 1346–1360.

Hwang, P. A., and W. J. Plant (2010), An analysis of the effects of swell and surface roughness spectra on microwave backscatter from the ocean, *J. Geophys. Res.*, *115*, C04014, doi:10.1029/2009JC005558.

Isoguchi O. and M. Shimada (2009), An L-Band Ocean Geophysical Model Function Derived From PALSAR, *IEEE Trans. Geosci. Remote Sens.*, *47*, 1925–1936.

Long, C. E., and D. T. Resio (2007), Wind wave spectral observations in Currituck Sound, North Carolina, *J. Geophys. Res.*, *112*, C05001, doi:10.1029/2006JC003835.

Longuet-Higgins and Stewart (1960), Changes in the form of short gravity waves on long waves and tidal currents, *J. Fluid Mech.*, *4*, 565–583.

Phillips, O. M. (1958), The equilibrium range in the spectrum of wind generated waves, *J. Fluid Mech.*, *4*, 426–434.

Rascle, N., F. Ardhuin (2012), A global wave parameter database for geophysical applications. Part 2: Model validation with improved source term parameterization, *Ocean Modelling*, *70*, 174–188, doi:http://dx.doi.org/10.1016/j.ocemod.2012.12.001.

Resio, D. T., C. E. Long, and C. L. Vincent (2004), Equilibrium-range constant in wind-generated wave spectra, *J. Geophys. Res.*, *109*, C01018, doi:10.1029/2003JC001788.

Saha, S., Moorthi, S., Pan, H.-L. et al (2009), The NCEP climate forecast system reanalysis, *Bull. Amer. Meterol. Soc.*, *91*, 1015–1057.

Sahlée, E., W. M. Drennan, H. Potter, and M. A. Rebozo (2012), Waves and air-sea fluxes from a drifting ASIS buoy during the Southern Ocean Gas Exchange experiment, *J. Geophys. Res.*, *117*, C08003, doi: 10.1029/2012JC008032.

Sampe, T., and S. Xie (2007) Mapping high sea winds from space: A global climatology, *Bull. Amer. Meteorol. Soc.*, *88*, 1965–1978, doi:http://dx.doi.org/10.1175/BAMS-88-12-1965.

Smedman, A., X. G. Larsén, and U. Högström (2003), Effect of sea state on the momentum exchange over the sea during neutral conditions, *J. Geophys. Res.*, *108*(C11), 3367, doi: 10.1029/2002JC001526.

Tamura, H., T. Waseda, Y. Miyazawa, and K. Komatsu (2008), Currentinduced modulation of the ocean wave spectrum and the role of nonlinear energy transfer, *J. Phys. Oceanogr.*, *38*, 2662-2684, doi:10.1175/2008JPO4000.1.

Tamura, H., T. Waseda, and Y. Miyazawa (2010), Impact of nonlinear energy transfer on the wave field in Pacific hindcast experiments, *J. Geophys. Res.*, *115*, C12036, doi: 10.1029/2009JC006014.

Thomson, J., E. A. D'Asaro, M. F. Cronin, W. E. Rogers, R. R. Harcourt and A. Shcherbina (2013), Waves and the equilibrium range at Ocean Weather Station P, *J. Geophys. Res.*, *118*, 5951–5962, doi:DOI: 10.1002/2013JC008837.

Toba, Y. (1973), Local balance in the air-sea boundary processes III. On the spectrum of wind waves, *J. Oceanogr. Soc. Japan*, *29*, 209–220.

Tolman, H. L., and D. V. Chalikov (1996), Source terms in a third-generation wind wave model, *J. Phys. Oceanogr.*, *26*, 2497–2518.

Tolman, H. L. (2009), User manual and system documentation of WAVEWATCH III TM version 3.14, Natl. Cent. for Environ. Predict., Natl. Weather Serv., NOAA, Camp Springs, Md.

Van Vledder, G. P. (2006), The WRT method for the computation of nonlinear four-wave interactions in discrete spectral wave models, *Coastal Eng.*, *53*, 223-242.

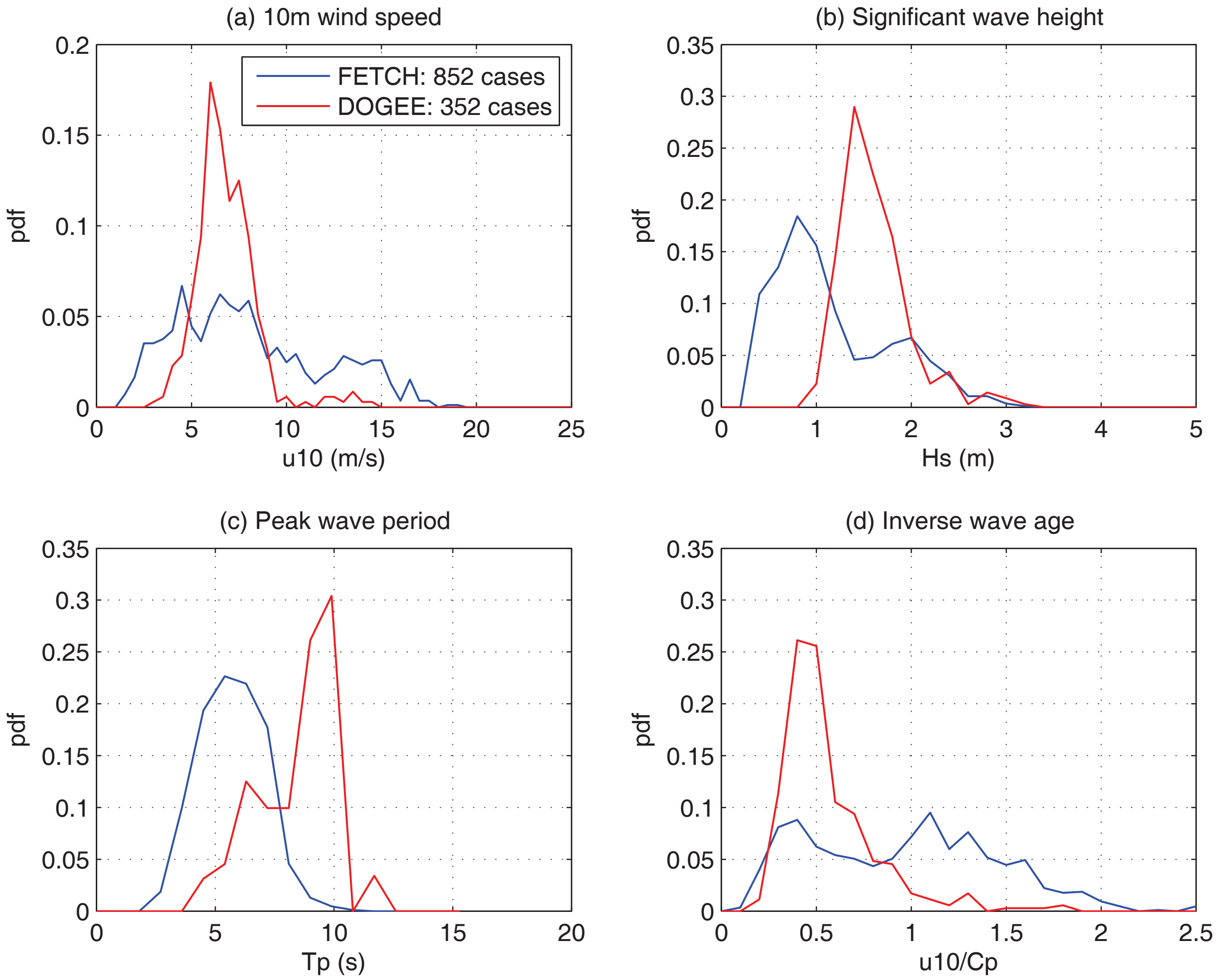

**Figure 1.** Probability density functions of observed wind and wave statistics: (a) surface wind at a height of 10 m, $U_{10}$; (b) significant wave height, $H_s$; (c) peak wave period, $T_p$; and (d) inverse wave age, $U_{10}/c_p$, where $c_p$ is the spectral peak phase speed. Blue and red lines indicate the datasets for FETCH (852 cases) and DOGEE (352 cases), respectively.

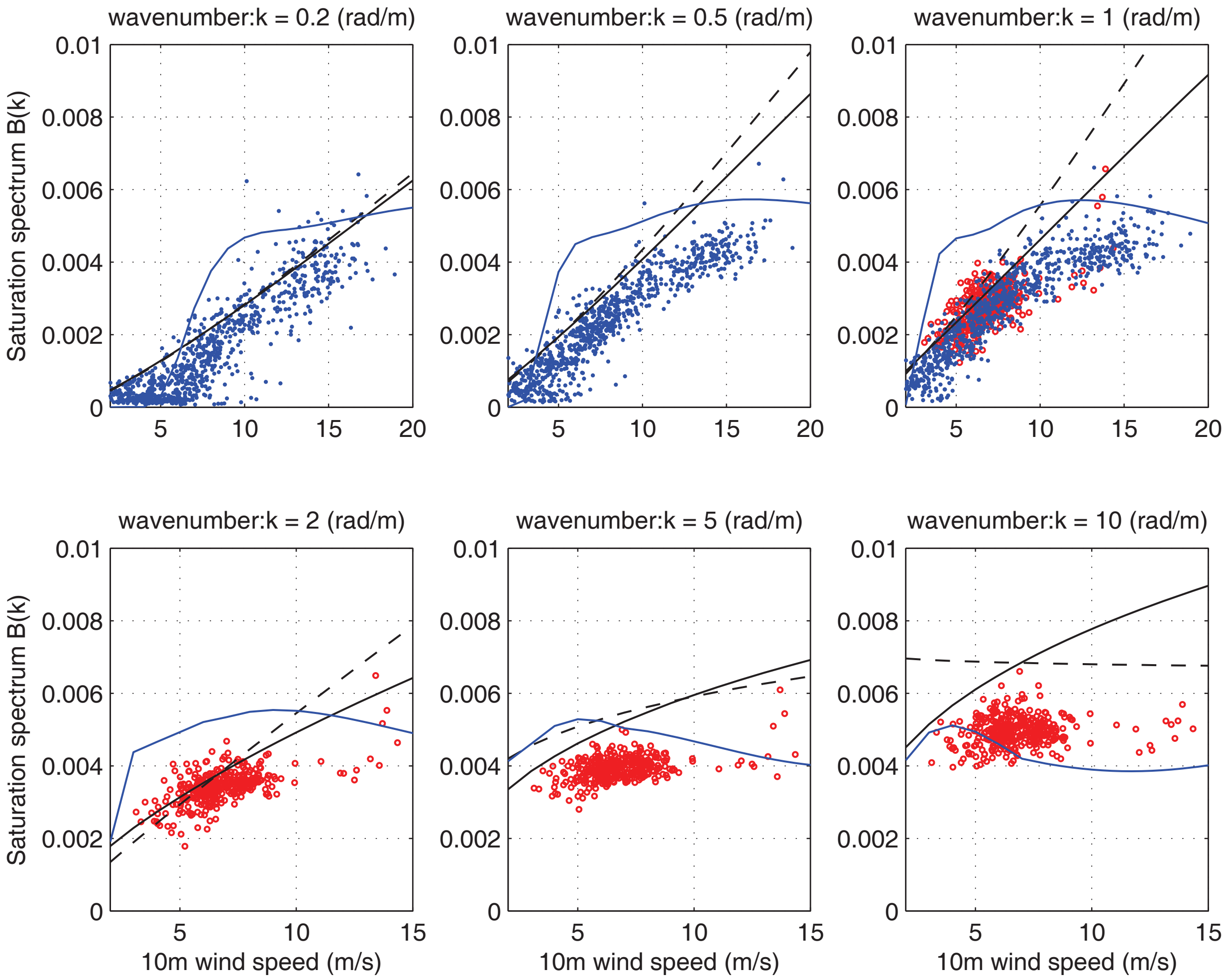

**Figure 2.** Saturation spectra, $B(k)$, plotted against wind speed for six different wavenumbers (0.2, 0.5, 1.0, 2.0, 5.0, and 10.0 rad/m). Blue dots show the observed $B(k)$ values for FETCH and red circles represent DOGEE. The $B(k)$ models proposed by *Hwang* [2008] with swell effect (H4 spectrum: dashed lines) and without swell effect (H1 spectrum: solid lines) are also compared. Blue lines show the *Elfouhaily et al.* [1997] spectrum (E spectrum).

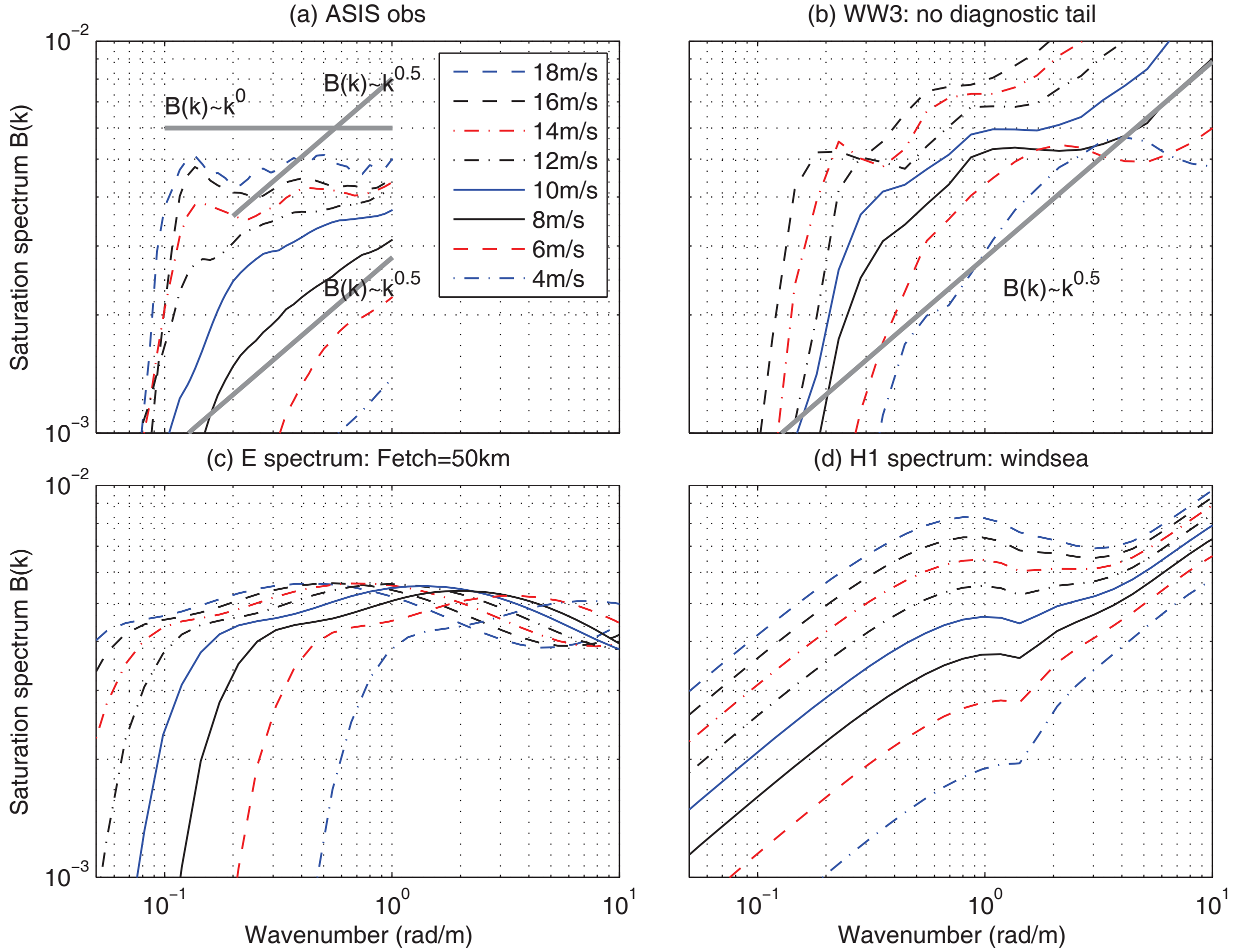

**Figure 3.** The mean saturation spectra for each wind speed range during the FETCH experiment. $B(k)$ is averaged in the wind speed bins (± 1 m/s) indicated in the legend. (a) ASIS observations ($k$: 0.05-1 rad/m) with reference power laws (gray lines) by *Phillips* [1958] ($B(k) \sim k^0$) and *Toba* [1973] ($B(k) \sim k^{0.5}$), (b) WW3 without the diagnostic tail, (c) *Elfouhaily et al.* [1997] for fetch=50 km (E spectrum), and (d) *Hwang* [2008] for windsea (H1 spectrum).

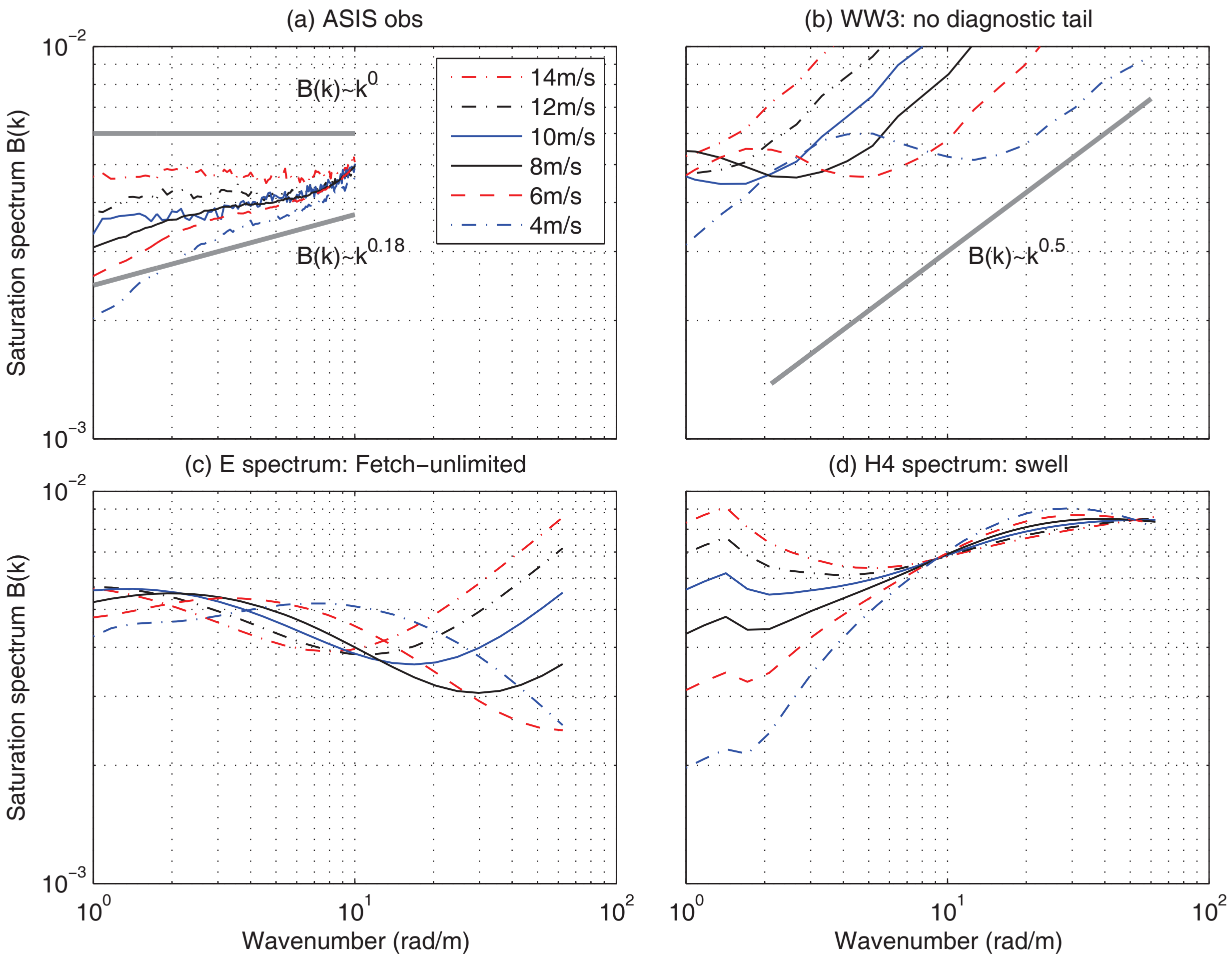

**Figure 4.** The mean saturation spectra for each wind speed range during the DOGEE. (a) ASIS observations ($k$: 1-10 rad/m) with reference power laws (gray lines) by *Banner et al.* [1989] ($B(k) \sim k^{0.09\pm0.09}$), (b) WW3 without the diagnostic tail, (c) *Elfouhaily et al.* [1997] for the fetch unlimited case (E spectrum), and (d) *Hwang* [2008] with swell effect (H4 spectrum).

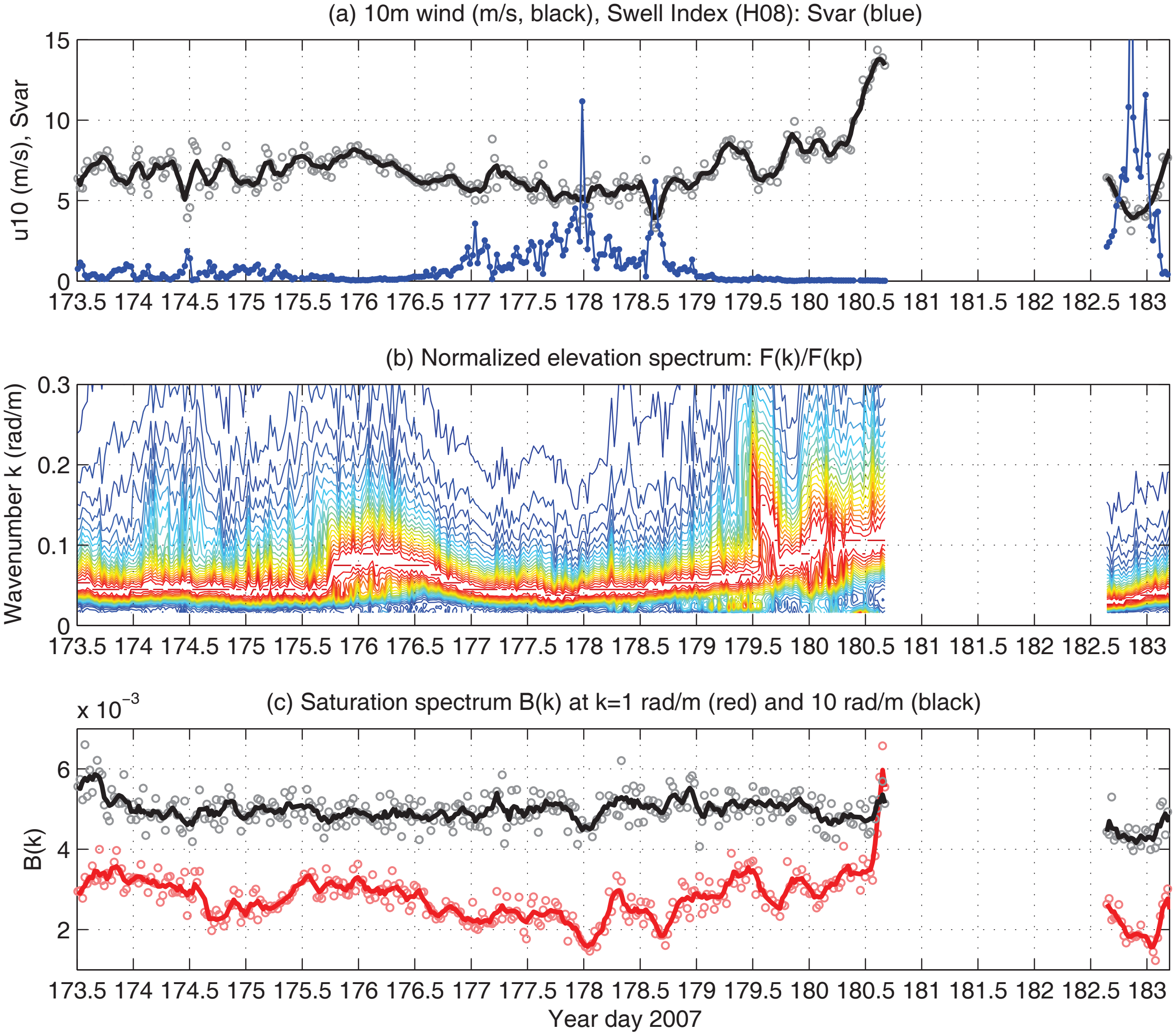

**Figure 5.** Temporal variation in wind and swell parameters retrieved from the DOGEE dataset; (a) $U_{10}$ and Swell index, *Svar*, proposed by *Hwang* [2008], (b) normalized elevation spectra in the lower wavenumber domain ($k$: 0-0.3 rad/m), which is estimated from the global wavelet spectrum, and (c) saturation spectra $B(k)$ at $k = 1$ rad/m (red; circles: 30-min average, thick line: 2.5 h running average) and at $k$=10 rad/m (black).

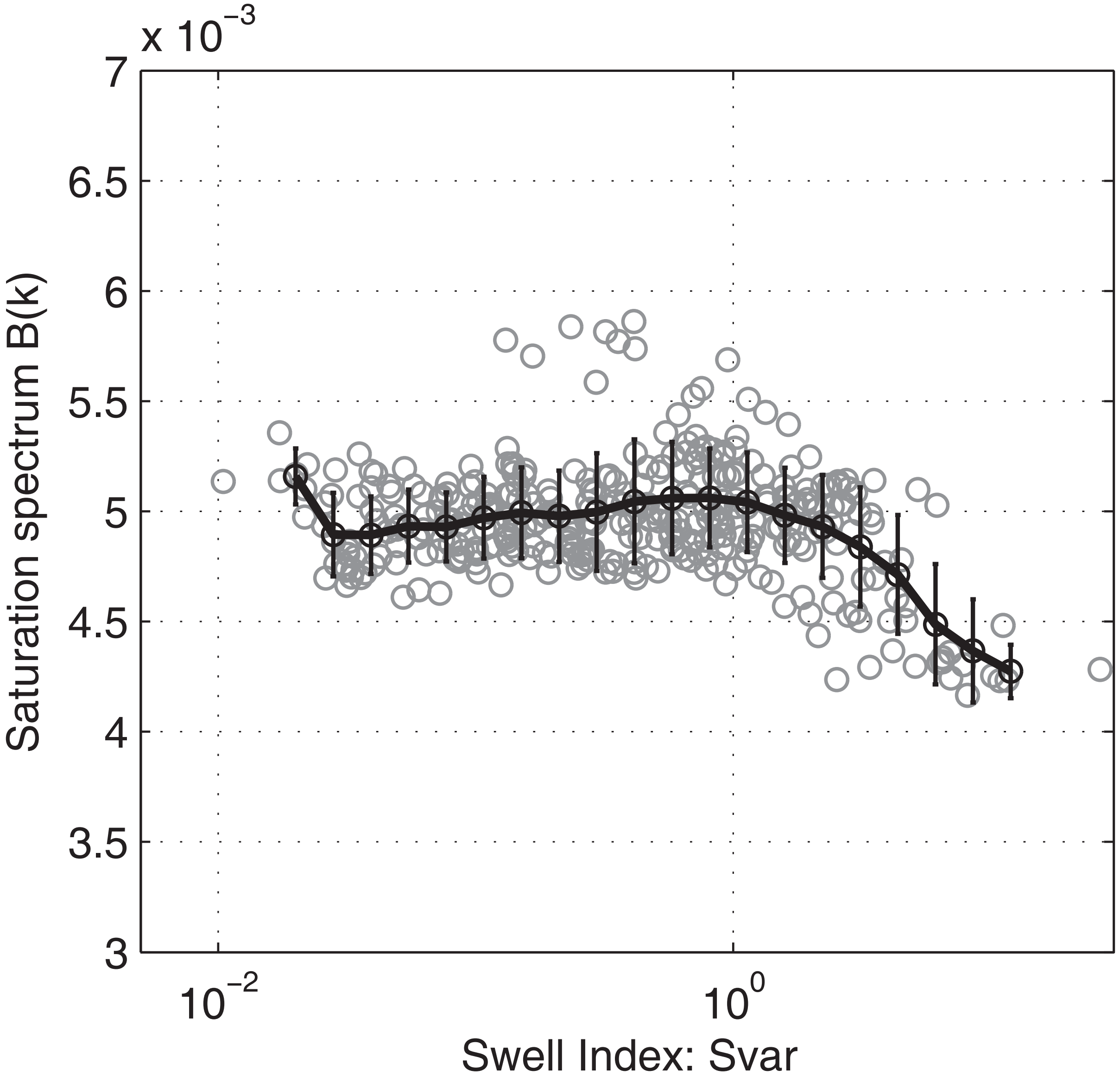

**Figure 6.** Scatterplot of the swell index, $Svar$, and the 2.5 h running average $B(k)$ at $k$=10 rad/m (gray circles). The black curve with bars shows the bin-averaged $B(k)$. The error bars correspond to one standard deviation.

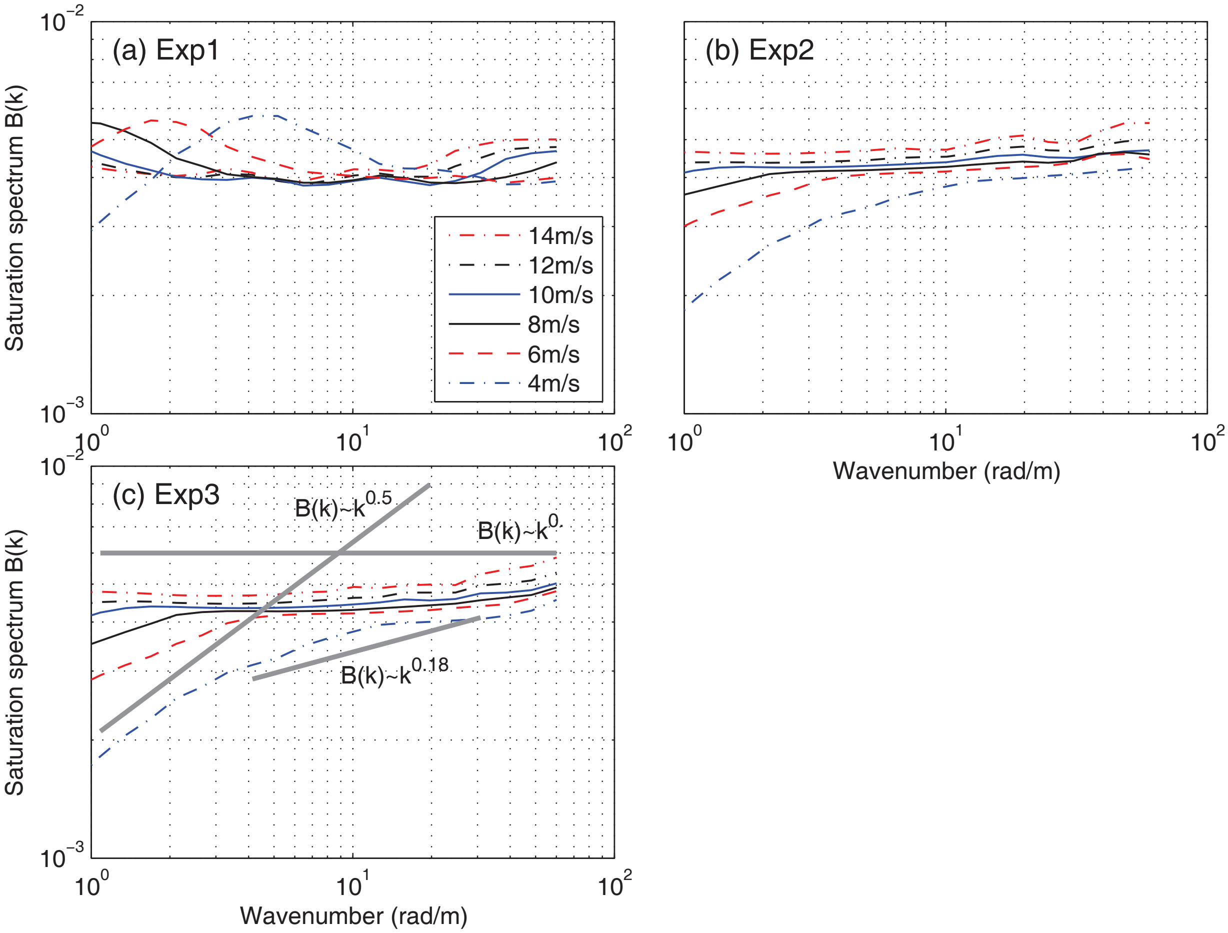

**Figure 7.** The mean saturation spectra $B(k)$ with nonlinear dissipation terms. (a) Exp1: $S_{in}^{TC96} + S_{ds}^{mTC96} + S_{nl}^{DIA}$, (b) Exp2: $S_{in}^{TC96} + S_{ds}^{D01} + S_{nl}^{DIA}$, and (c) Exp3: $S_{in}^{TC96} + S_{ds}^{D01} + S_{nl}^{WRT}$.

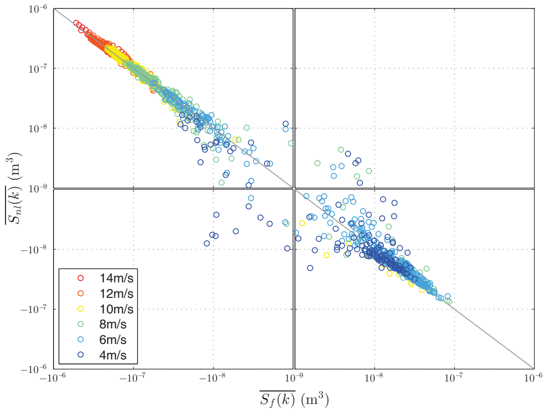

(a) wavenumber range: 1–2 rad/m

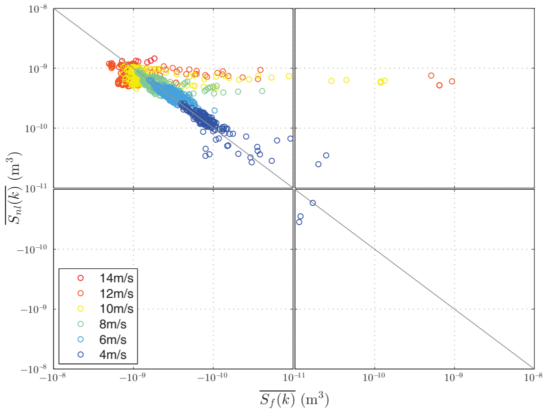

(b) wavenumber range: 10–20 rad/m

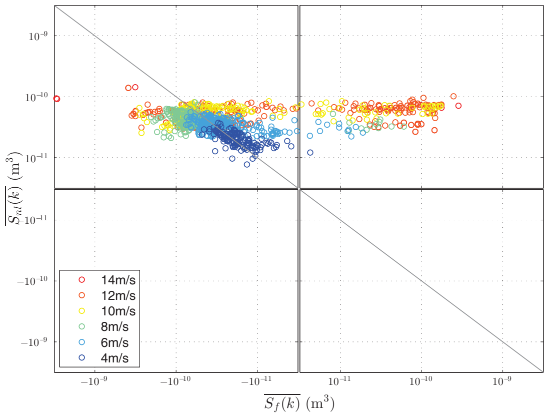

(c) wavenumber range: 30–40 rad/m

**Figure 8.** Scatterplot of the net external force, $S_f$, and the nonlinear transfer, $S_{nl}$, which were averaged in the wavenumber bins, (a) $k$:1-2 rad/m, (b) $k$:10-20 rad/m and (c) $k$:30-40 rad/m. The circles are color-coded according to the surface wind speed, $U_{10}$.

(a) wavenumber range: 1–2 rad/m

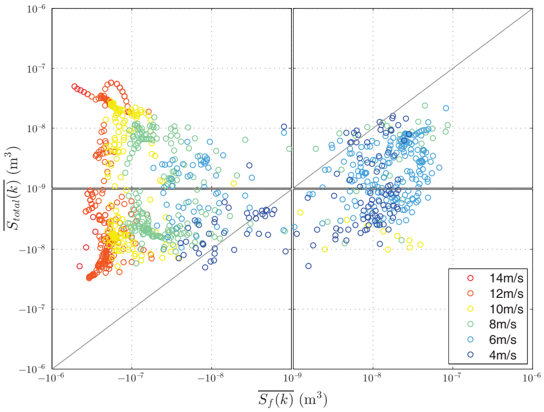

(b) wavenumber range: 10–20 rad/m

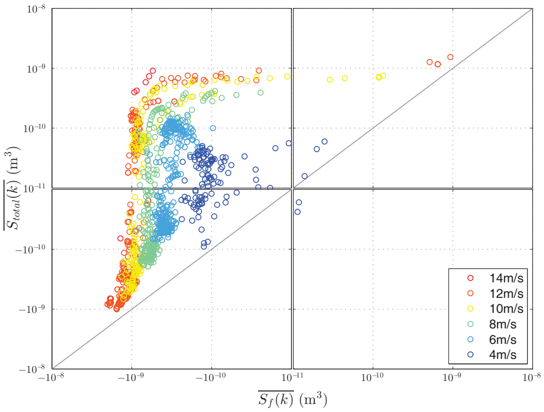

(c) wavenumber range: 30–40 rad/m

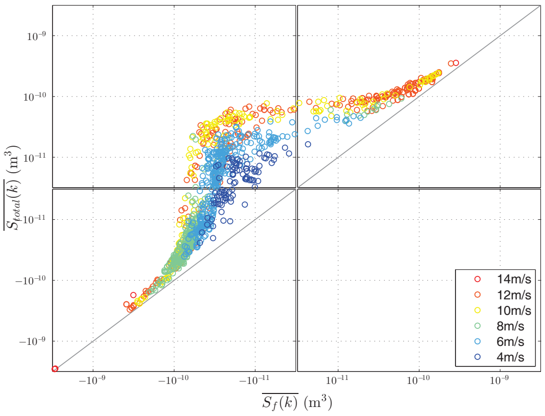

**Figure 9.** Scatterplot of the net external force, $S_f$, and the total source, $S_{total}$, which were averaged in the wavenumber bins, (a) $k$:1-2 rad/m, (b) $k$:10-20 rad/m and (c) $k$:30-40 rad/m. The circles are color-coded according to the surface wind speed, $U_{10}$.

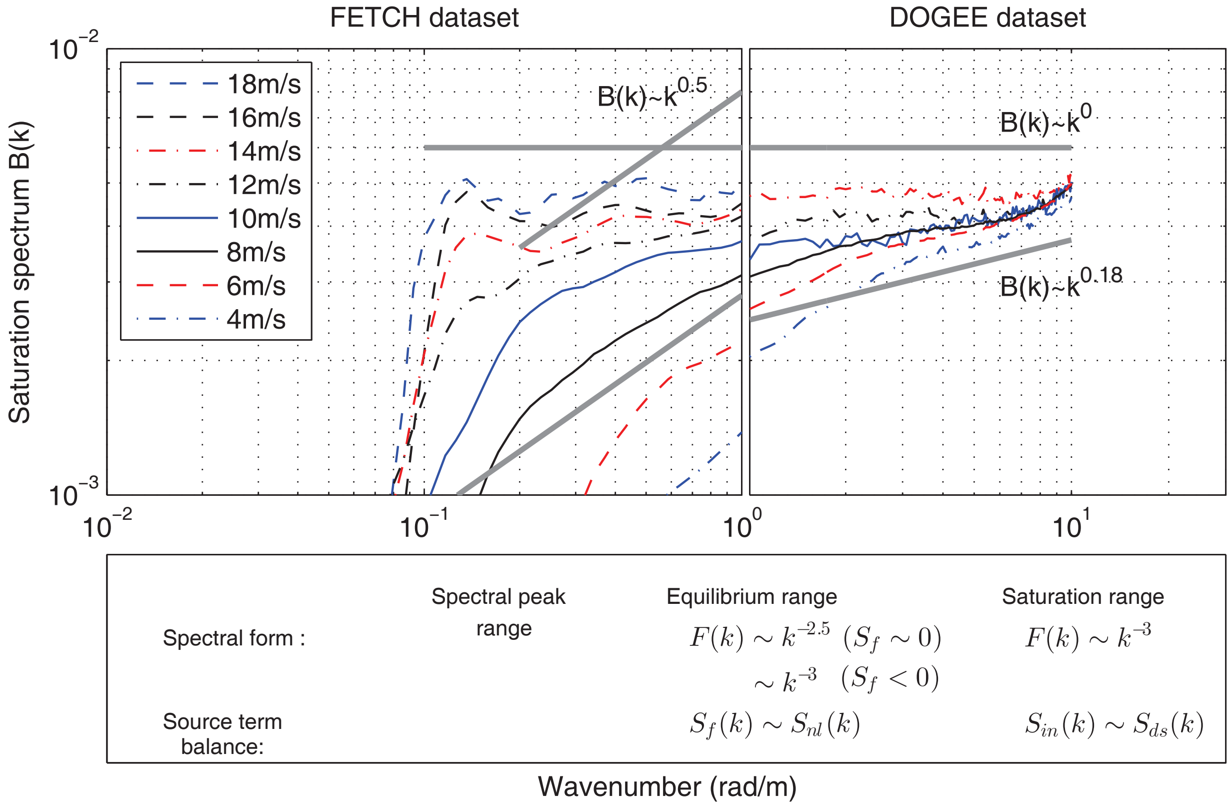

**Figure 10.** Schematic diagram of the spectral structure and source term balance in the equilibrium and saturation ranges.

**Table 1.** Design of hindcast experiments for FETCH and DOGEE

| Hindcast experiments | Computational domain | Horizontal resolution | Computational period |
|---|---|---|---|
| FETCH | 37°N-44°N, 0°-13°E<br>(Western Mediterranean) | 0.05° | 1998/03/01-1998/05/01 |
| DOGEE | 0°-70°N, 100°W-15°E<br>(North Atlantic) | 0.2° | 2007/05/01-2007/08/01 |